Open Access

Catalysis Research

LIDSEN Publishing Inc.

Research Article

Impact of Pt-Ni Nanoparticle Architecture on Electrocatalytic Oxidation Reaction in Fuel Cells

Nicolas A. Ishiki [1, 2], Maria L. Della-Costa [1], Beatriz Keller [1], Kleper O. Rocha [1], Francielle Bortoloti [1], Antonio C. D. Ângelo [1, *]

1. Electrocatalysis Laboratory, Faculty of Science, State University of São Paulo (UNESP), Bauru, SP, Brazil; E-Mails: nicolas-ishiki@usp.br; maria.laura@unesp.br; beatriz.keller@unesp.br; kleper.rocha@unesp.br; francielle.bortoloti@unesp.br; ac.angelo@unesp.br
2. Electrochemistry Group, Institute of Chemistry of São Carlos, University of São Paulo (USP), São Carlos, SP, Brazil

* **Correspondence:** Antonio C. D. Ângelo; E-Mail: ac.angelo@unesp.br

Academic Editor: Wei Wang

Special Issue: Recent Advances in Pt-Based Catalysts

Catalysis Research
2023, volume 3, issue 4
doi:10.21926/cr.2304027

Received: September 04, 2023
Accepted: November 09, 2023
Published: November 16, 2023

Abstract

This paper investigates how the aggregation of bimetallic nanoparticles (NPs) influences the electronic condition of the surface adsorption site and, hence, the performance of materials during the electrooxidation of fuels in an alkaline medium. First, we synthesized Pt-Ni NPs in three configurations: ordered intermetallic, ordinary alloy, and core-shell. The NPs contained Pt and Ni close to a 1:1 Pt/Ni atomic ratio. They had similar particle sizes, which allowed us to evaluate their performance without the influence of these physical parameters. Depending on the structural arrangement of the Pt and Ni atoms in the NP, the electronic condition of the surface adsorption site (Pt) changed significantly. Consequently, the performance of the materials varied whenever they were used as anode material for the electrooxidation of hydrogen, methanol, ethanol, ethylene glycol, and glycerol in an alkaline solution. The electronic condition of the surface site strongly affected the adsorption characteristics of the reactants, intermediates, and products, consequently impacting the material's performance

during the electrochemical processes. The approach adopted here could contribute to a better understanding of electrocatalytic processes and the design of selective electrocatalysts.

Keywords
Nanostructure; electrocatalysis; fuel cell; platinum-nickel; electronic state

1. Introduction

Electrocatalysts still lack a consistent guideline that can reliably provide the fundamental basis for the development of active materials and for understanding their performance in electrocatalytic processes. Pursuing a correlation between the characteristics of a specific material and its electrochemical activity remains the main goal in this area. Although the electrochemical activity of a material is always attributed to its geometric (structural) and electronic properties, no sufficient explanation for this phenomenon has been provided because it is difficult to split these two contributions as they intrinsically depend on each other.

There is some evidence that the structural arrangement of species in a catalyst matrix influences the activity of the catalyst toward a given electrode reaction. The following are the most representative studies regarding this subject. Alayoglu *et al*. [1] investigated the activity of Ru@Pt core-shell nanoparticles (NPs) toward the oxidation of carbon monoxide (CO) in hydrogen (H_2). These authors synthesized and evaluated three different structural arrangements of Ru-Pt NPs: ordinary alloy, Ru@Pt core-shell, and linked monometallic. The authors noticed that the core-shell structure presented outstanding performance and suggested that this arrangement played an essential role in the activity toward CO oxidation. The same research group [2] used the Rh-Pt bimetallic system in a similar research approach. The authors reported that the materials displayed markedly different catalytic activities despite having similar size, composition, and surface area. Improved activity has been attributed to changes to the architectural configurations of materials, which altered the electronic structure of the surface metal and facilitated the reaction compared to Pt NPs. The authors did not explore more detailed explanations of the phenomenon, but it was strongly evident that the structural configuration of the catalyst affected the activity toward the investigated reaction. Liu and Eichhorn [3] evaluated intermetallic, core-shell, and alloy Pt-Sn NPs as CO-tolerant electrocatalysts for H_2 oxidation. They confirmed that the intermetallic was highly stable during the potential cycling of PtSn@Pt core-shell NPs in the presence of CO. Once again, it was verified that distinct nanoparticle structures elicited different activities.

Pt-Ni structures have long been at the forefront of catalyzing the oxygen reduction reaction (ORR) at the cathode of fuel cells (FCs) [4]. Interestingly, these same metallic compositions have exhibited intriguing activity for electrooxidation reactions [5, 6]. These configurations resulted in the study of Pt-Ni materials as electrocatalysts for both responses, such as the hydrogen oxidation reaction (HOR) and/or alcohol oxidation, in conjunction with ORR [7, 8]. While this multifunctional performance is indeed remarkable at first glance, it should be noted that these reactions often occur in the same potential region, resulting in similar intrinsic electronic transitions. Consequently, numerous efforts have been dedicated to enhancing the performance of Pt-Ni electrocatalysts by carefully architecting the atomic arrangement within the crystallographic lattice [5, 9, 10]. For instance, Bao

et al. [5] conducted a comprehensive study on Pt-Ni nanoparticles with nominal atomic ratios of 1:1, 2:1, and 3:1 using X-ray absorption spectroscopy (XAS). Their investigation revealed distinct variations in the intensities of the white lines concerning pure Pt and Ni, which were attributed to the varying degrees of oxidation configurations of these materials, which played a pivotal role in dictating their performance in methanol oxidation. Notably, they emphasized that the geometric effect appeared to influence observed catalytic performance significantly more than the electronic effect. Although the papers above clearly pointed to the probable relationship between the structural arrangement of the electrocatalyst and its implementation, this issue still requires elucidation.

In a recent paper, we synthesized and fully characterized a bimetallic material (Pt-Sn) in three distinct structural nanoparticle arrangements (ordered intermetallic, alloy, and core-shell) [11]. Then, we proposed that the electronic condition of the surface adsorption site was related to the interaction of the material. More specifically, we proposed that the electrochemical potential of the surface adsorption site could be described as:

$$\mu_e^\alpha = \mu_c^\alpha + z \times F \times \emptyset \quad (1)$$

Where μ_e^α is the electrochemical potential of the species in phase α; μ_c^α it is the chemical potential of the same species in the same phase; z is the charge;F is the Faraday constant; and $\emptyset$ is the potential where the species is located (which can be later related to the electrode's potential). Regarding a species at the surface active site, the electrochemical potential of this species can be considered as the ability of the surface site to be active for a given electrochemical process. The chemical potential μ_c^α it depends on the species' intrinsic nature and the chemical environment where it is inserted.

$$\mu_c^\alpha = \mu^0 + \chi_{int}^\alpha \quad (2)$$

Where μ^0 represents the intrinsic chemical ability (chemical nature) of the species and χ_{int}^α it is the ability of the species to interact with the environment.

Deeper analysis of Equations (1) and (2) provided the relation of the chemical potential of the active site with the environment where it is located and, therefore, its electrochemical potential. In this approach, we proposed that the species on the surface of materials with distinct structures such as ordered intermetallic, alloy, and core-shell should display different binding energies, which would impact the electronic density of the adsorption site of the noble metal and hence the electrochemical potential of the species on the surface active site. This is a vital characteristic for the adsorption of reactants, intermediates, and products since it could affect the adsorption energy of these species. We hypothesized that the environment around the surface adsorption site could influence its electrochemical potential. For the same chemical identity, stoichiometric proportion, and NP size, we found that the electronic density of the surface adsorption site (Pt) could vary substantially depending on the neighborhood arrangement. We proposed that this phenomenon could be caused by the energy involved in the Pt-M interaction, which should rely on the material's nanostructure.

The electronic condition of the surface adsorption site has a crucial part in the electrode process: this condition can determine the adsorption energy of the reactants, intermediates, and products, thereby impacting the completion of the process. In the case of electrooxidation reactions involved

in FCs, such as proton-exchange membrane (PEM) and anion-exchange membrane (AEM), the adsorption of these species and even contaminants often determine the reaction mechanism pathways and usually define whether a device is successful. Whenever hydrogen gas is used as fuel in FCs and obtained from the reforming of organic compounds, it can be contaminated with traces of CO, which can irreversibly adsorb on the catalyst's surface. Consequently, the surface is deactivated for further steps of the electrode process. The electrooxidation of methanol proceeds via two different pathways. One has an essential contribution from the CO intermediate adsorbed on the catalyst's surface [12-15]. When it comes to the electrooxidation of ethanol and other polyalcohols like ethylene glycol and glycerol, additional difficulties arise, including cleavage of the C-C bond and extraction of the most electrons per molecule. These reactions commonly culminate in partially oxidized products, which decreases the efficiency of the electrochemical process [16-23]. In all these examples, the electrode material influences the reaction using a third body effect, bifunctional action, electronic characteristic of the surface site (actual electrocatalytic result), or even a combination. Thus, laboratories worldwide have been committed to developing new electrocatalysts (or improving existing ones) to enhance the processes. Nevertheless, how to design electrocatalysts that can overcome these constraints is unknown.

In the present paper, we present the results concerning the synthesis, characterization, and electrochemical evaluation of Pt-Ni system NPs in the ordered intermetallic, ordinary alloy, and core-shell architectural arrangements with the same stoichiometric composition and similar particle sizes. We evaluate the performance of these materials as anode toward the electrooxidation of hydrogen, methanol, ethanol, ethylene glycol, and glycerol in an attempt to establish a proper connection between the adsorptive characteristics and the effectiveness of the electrochemical process. More specifically, we aimed to investigate how much the structure of the material and the electronic condition of the surface adsorption site influences each electrode reaction, in order to understand how the electrochemical process depends on the properties of the electrode composition.

2. Materials and Methods

Pt-Ni materials with 1:1 nominal composition were synthesized in three structural architectures: ordered intermetallic, ordinary alloy, and core-shell NPs. The synthesis methods employed here have been reported in our previous work [11], but below, we briefly describe the main steps for better understanding the research developed herein.

Commercially available Pt/C (E-TEK, mean size 2-3 nm) was used for comparison. All the materials were anchored on Carbon black (Vulcan XC72, Cabot®) previously treated at 400°C for 4 h under an inert N_2 (White Martins, 5.0) atmosphere. The carbon black/metal ratio was 80:20, resulting in a metal loading of 20 wt. % M/C, divided into 10 wt. % Pt and 10 wt. % Ni.

To synthesize the ordered intermetallic PtNi/C NPs, Cable and Schaak suggested the polyol reduction process [24] with a few modifications. First, the carbon support was dispersed in tetra ethylene glycol (TEG, Sigma-Aldrich, 99%) and solubilized in the same solution together with appropriate amounts of chloroplatinic acid hexahydrate (Sigma-Aldrich), tetra-hydrated nickel (II) acetate (Sigma-Aldrich), polyvinyl pyrrolidone (PVP, Sigma-Aldrich), polyamine (Sigma-Aldrich, 70%), and oleic acid (Sigma-Aldrich) under ultrasonic shaking. A reflux setup was used to de-aerate (N_2, White Martins, 5.0) and homogenize the mixture for 45 min. Next, sodium borohydride (Sigma-

Aldrich, 98%) TEG solution was slowly added to the mix, which was kept under reflux at 260°C for 4 h. The resulting product was sequentially washed by centrifugation (Excelsa®, II Centrifuge, Model 2006BL) with acetone (Dinamica), ethanol (Merck, 96%), and deionized water (Deionizer Synergy UV, Millipore, 18.3 MΩ). The solid was dried at 60°C and thermally treated at 300°C for 1 h under N_2 atmosphere to remove organic residues that eventually remained on the product.

The PtNi/C alloy NPs were obtained with a dispersion of the carbon support in deionized water and added to a tetra-hydrated nickel (II) acetate aqueous solution. The surfactants sodium dioctylsulfoccinate (Sigma-Aldrich, 98%), oleic acid, and polyamine were solubilized in h-heptane (Merck, 99%). Then, both solutions were mixed and vigorously stirred, and sodium borohydride and chloroplatinic acid hexahydrate (Sigma-Aldrich) were added. The reaction vessel was stirred at room temperature for 12 h. The resulting product was washed with ethanol, acetone, and deionized water. The solid was dried at 60°C in an oven and thermally treated at 300°C for 1 h, as described previously.

Ni@Pt core-shell NPs were produced using the modified polyol method proposed by Chen and co-workers [25]. The carbon support was dispersed in TEG, and the dispersion was de-aerated with N_2 for 20 min and kept under constant stirring. After that, sodium hydroxide (Merck) and nickel (II) acetate were added to the solution with oleic acid and polyamine. The temperature of the solution was raised to 138°C, and sodium borohydride TEG solution was added. Finally, chloroplatinic acid hexahydrate TEG solution was added, stirring the system for 60 min. The resulting product was washed, dried, and thermally treated for the other synthesized materials.

The products were fully characterized by X-ray diffraction (XRD), Energy Dispersive X-ray spectrometry (EDX), High-Resolution Transmission Electron Microscopy (HRTEM), and X-ray absorption Spectroscopy (XAS) on Near Edge (XANES) region. XRD was conducted on a RIGAKU MiniFlex 600 Diffractometer with a Cu cathode radiation (λ = 1.5406 Å) source that generated 40-kV and 15-mA radiation. The diffractograms were recorded for 2θ values ranging from 20 to 90° at 10°/min, with steps of 0.04°. EDX was accomplished with a Zeiss Electronic Microscope, model LS-15 Evo, operating at 15 kV and equipped with an EDX detector from Oxford Instruments. The work distance varied from 8 to 10 mm. Five distinct points were examined on each material sample. The HRTEM images were recorded with an FEI TECNAI G_2 F200 transmission electron microscope operating at 200 kV and equipped with a Gatan camera. The X-ray absorption Pt L3 near edge (11.564 eV) spectra were obtained in the light beam D06A-DXAS at the Synchrotron Laboratory (LNLS, Campinas, BRAZIL). The shaft had a (111) Si monochromator and CCD solid-state detector. The powdered samples were cold pressed on a carbon tissue and mounted in an acrylic electrochemical cell specially designed for XANES essays. The electric contact with the working electrode was achieved by means of an Au wire. A Pt gauze with a high surface area was used as the counter electrode. The potential of the electrode was monitored via a Reversible Hydrogen Electrode (RHE) with a 302N Autolab Potentiostat. At room temperature, 0.5 mol L^{-1} KOH (Merck, ≥85%) solution was employed as the electrolytic solution.

The materials were evaluated as anode for the oxidation of liquid fuels methanol (Merck, ≥99.5%), ethanol (Merck, ACS), ethylene glycol (Fluka, ≥99,5%), and glycerol (Sigma, ≥99%) using the cyclic voltammetry (CV) and chronoamperometry (CA) techniques. To this end, an aqueous dispersion of the supported material, isopropyl alcohol (Sigma-Aldrich), and Nafion® 117 solution (Aldrich) were deposited as a thin film on a vitreous carbon surface. The suspension was prepared using 10 mg of the synthesized catalysts + 20 µL Nafion solution + 0.39 mL isopropyl alcohol + 1.6 mL deionized water. This suspension was sonicated by 45 minutes for homogenization. Afterward, 10 µL of the

prepared solution was applied to the previously polished vitreous carbon (diamond paste, Arotec 0.25 µm) and dried in air at room temperature. After drying, the resulting surface was electrochemically characterized in 0.5 mol L^{-1} KOH solution and evaluated for fuel oxidation in 0.5 mol L^{-1} KOH + 0.5 mol L^{-1}—fuel solution at room temperature. The Rotating Disc Electrode (RDE) technique was employed to study the Hydrogen Oxidation Reaction (HOR) data. The answers were degassed by bubbling or passing N_2 through or over the solution before and during the experiments. The electrolyte solution was saturated in hydrogen gas after the resolution was degassed under N_2 flow. Three electrode configurations were tested as anode. A high-surface Pt wire was used as the counter electrode, and the RHE was employed as the reference electrode. The techniques were applied via the Nova® Electrochemical Software through a 302N AutoLab Potentiostat. More specific experimental conditions will be presented when necessary during the discussion of the data.

3. Results

3.1 Ex-Situ Characterization

PtNi/C ordered intermetallic was first characterized by X-ray techniques (Figure 1). Figure 1A reproduces the XRD profile obtained for this material, where the peaks at 2θ = 41°, 48°, 70°, and 84° coincided with the four most intense peaks found in the crystallographic file for intermetallic Pt-Ni material (#AL2798), with slight displacements. According to the file, these peaks correspond to planes (111), (200), (220) and (311), respectively. The results presented in this study align with the XRD profile previously reported by DiSalvo *et al.* [9] for intermetallic Pt-Ni. However, given the tiny particles observed in their material, they decided to conduct a 24-hour annealing process at a higher temperature, increasing the particle size from *ca*. 2-4 nm to 15-20 nm. This growth allowed new peaks related to other crystallographic planes to be visualized. A similar procedure was adopted by Zou *et al*. [10] with a thermal treatment of 500-600°C for 5-20 h. We did not treat the material in these conditions since this method could dramatically alter the NP size, which we consider a significant variable to compare with the other structures under study. Figure 1B depicts the micrograph of the Pt-Ni-ordered intermetallic material obtained by the HRTEM technique. The graph inset shows the histogram of the particle size of this material, which is close to an average of 2 nm each. Besides that, in the same experiment, we obtained the particle electron diffraction pattern (Figure 1C), which was used to measure interplanar distances by Image J® software. For this ordered intermetallic material, the calculated distance was 0.215 nm, which we unambiguously assigned to the set of planes (111) for intermetallic Pt-Ni based on the Crystmet Database [26].

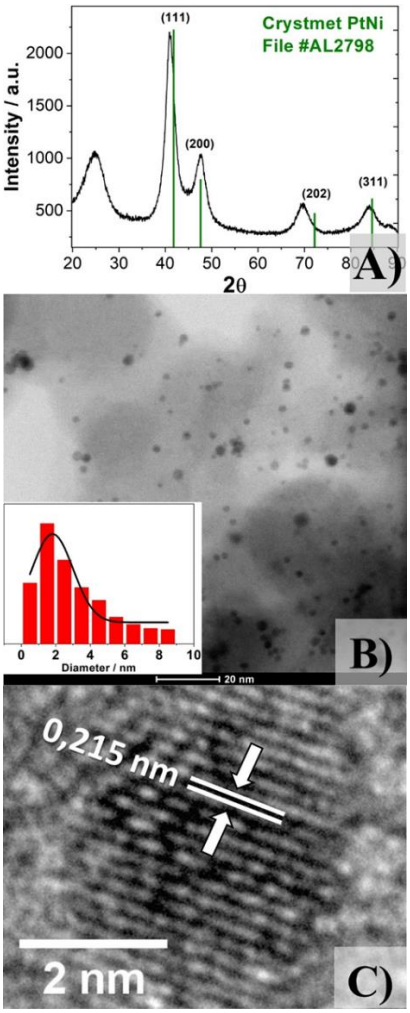

Figure 1 Characterization of PtNi/C Ordered Intermetallic arrangement by A) X-Ray diffractogram with the PtNi - File #AL2798 (Green); B) HR-TEM micrograph (graph inset present the size distribution histograms for the sample); and C) Particle electron diffraction.

Figure 2 shows the same results for PtNi/C alloy, which presents, at the XRD profile (Figure 2A), the characteristics peaks related to the planes (111), (200), (220), (311), and (222) at 2θ values of 40°, 46°, 68°, 83°, and 86°, respectively corresponding to face-centered cubic (FCC) Pt structure (#27852). The prominent peaks shifted to higher values, which suggested that a Pt-Ni alloy emerged [27]. The shift was due to the higher interaction between the Pt and Ni atoms in the lattice, which led to cell contraction as a result of the smaller size of the Ni atom (1.25 Å) as compared to Pt (1.39 Å) [28]. By using the peak corresponding to the (220) set of planes, we calculated the lattice parameter (α_{FCC}) for the Pt-Ni alloy by using Equation (3) [28] below:

$$\alpha_{FCC} = \frac{\lambda_{k\alpha 1} \times \sqrt{2}}{sen\theta_{max}} \quad (3)$$

Where α_{FCC} is the cell parameter considering the FCC cell; $\lambda_{k\alpha 1}$ is the wavelength of the radiation ($Cu_{k\alpha 1}$ = 1.54056 Å); and θ is the angle of radiation incidence on the sample. The α_{FCC} of the alloy was 3.88 Å, slightly smaller than the value reported in the literature [26].

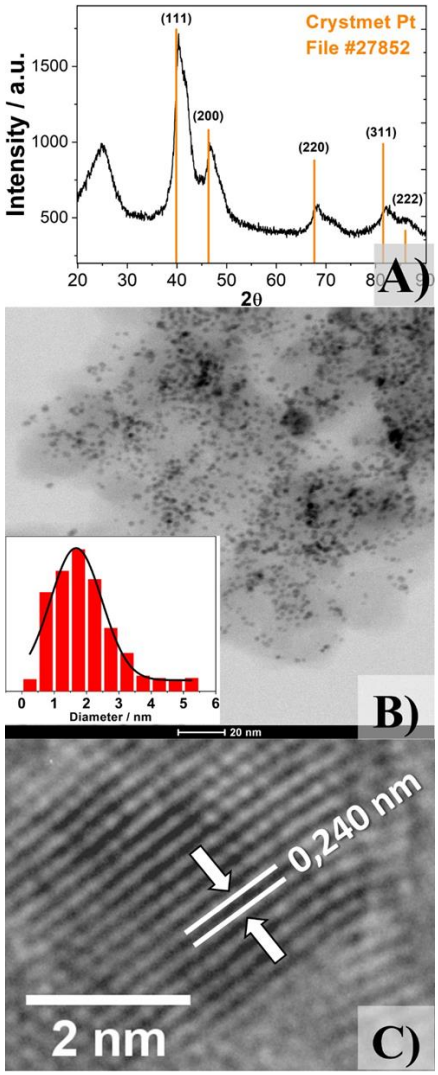

Figure 2 Characterization of PtNi/C Ordinary Alloy arrangement by A) X-Ray diffractogram with the PtNi - File #AL2798 (Orange); B) HR-TEM micrograph (graph inset present the size distribution histograms for the sample); and C) Particle electron diffraction.

Micrographs of the alloy material (Figure 2B) also showed good dispersion of the NPs at the carbon substrate and an average NP size close to 2 nm. The measured interplanar distance in Figure 2C revealed a value of 0.240 nm for the alloy, which could not be straightly assigned to any set of planes for Pt (#27852). However, it must be borne in mind that the introduction of Ni into the Pt lattice modified the interplanar distance considerably, as stated earlier in the discussion about the XRD measurements.

Finally, Figure 3 shows the results for core-shell material. Figure 3A contains the XRD profile for the core-shell Ni@Pt/C, and the peaks ascribed to the set of planes of the pure Pt FCC structure shifted to larger values of 2θ. When Alayoglu and Eichhorn [2] studied the formation of Rh@Pt, they observed that the shell peaks went according to the relative amount of Rh and Pt. This shift did not result from Pt-Rh alloying; it resulted from mass-averaged diffraction effects associated with the core-shell structure. Even with the synthesis in an inert atmosphere, peaks between 30 and 40° can be attributed to some oxides [25], probably formed by post-synthesis air exposure. Here, taking the

rise related to the plane (220) and again using Equation 3, we calculated the α_{FCC} for the Ni@Pt/C core-shell. Compared with the α_{FCC} of pure Pt (3.94 Å), the core-shell also showed the Pt lattice contraction to 3.85 Å, which will be discussed in the next section. Figure 3B shows that the Ni@Pt/C core-shell was the only structure slightly larger than the other configurations (~4 nm). The larger size of the core-shell was not that significant for comparison and was undoubtedly due to the preparation method, as stated in our previous publication [11]. By the pattern of particle electron diffraction of the core-shell material (Figure 3C), we obtained two values of interplanar distances: 0.226 nm for the outer portion of the particle and 0.203 nm for the inner part, which correspond respectively to the Pt and Ni lattices. We assigned these values to the set of planes (111) for both metals compared to the Pt (#27852) and Ni (#AL3274) files. These assignments corresponded to the 100% intensity peaks in the crystallographic database [26].

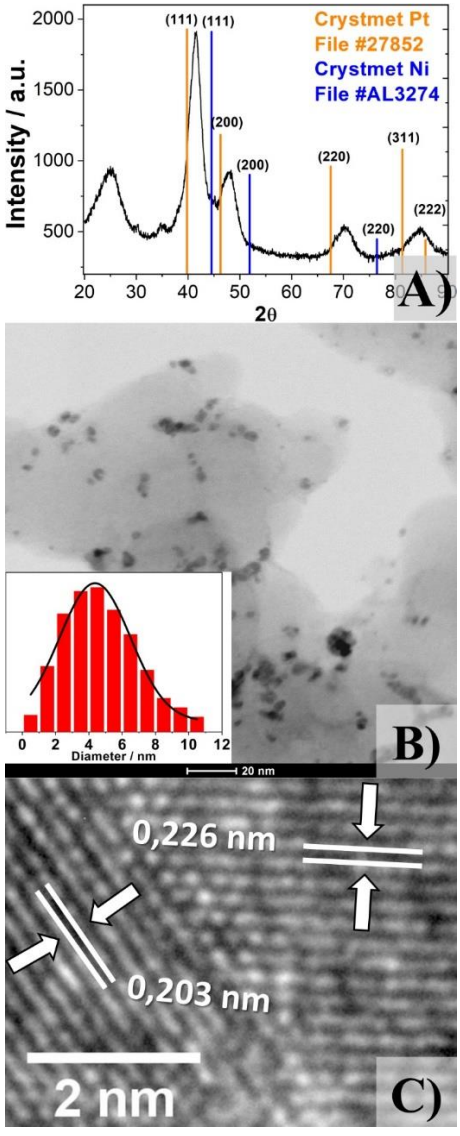

Figure 3 Characterization of Ni@Pt/C Core-Shell arrangement by A) X-Ray diffractogram with the Pt (Orange - #27852) and Ni (Blue - #AL3274) files; B) HR-TEM micrograph (graph inset present the size distribution histograms for the sample); and C) Particle electron diffraction pattern with the measured interplanar distances.

We conducted EDX assays for all the materials to estimate the Pt/Ni atomic proportion. The results are presented in Supporting Information (Figure S1), and the data showed the Pt: Ni ratios close to 1:1. The results are summarized in Table S1.

Some limitations are unavoidable with the *ex-situ* techniques, such as surface transformation and the possibility of oxide formation on the materials. In addition, the smaller size of the NPs creates another limitation: the low sensitivity of some techniques. Considering these variables, we expect that these materials will show more explicit differences by *in-situ* characterizations and electrochemical methods, which are very sensitive to the surface of the materials.

3.2 In-Situ Characterization

Figure 4 displays the cyclic voltammetry profiles recorded for the three Pt-Ni NP structures at 0.5 mol L^{-1} KOH solution and a scan rate of 50 mV s^{-1}. The profiles resembled the usual Pt NP profiles. The difference lay in the definition of the hydrogen adsorption/desorption peaks in the potential region around 0.2 V. Disregarding the common electrochemical issues of these electrode materials, the very close similarity between the capacitive current densities of the samples also indicated that the electrochemical areas available for the electrode processes were remarkably similar. As discussed earlier, this condition is crucial for a reliable comparison of the electrochemical properties of the materials based on their structures.

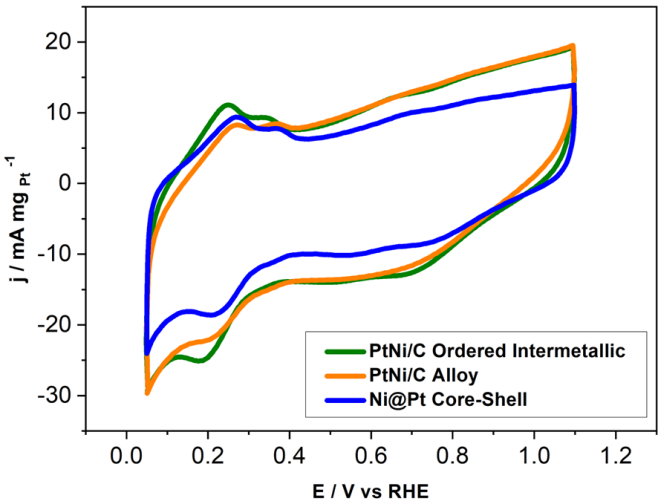

Figure 4 Cyclic voltammograms for PtNi/C Ordered Intermetallic (Green), PtNi/C Alloy (Orange) and Ni@Pt/C Core-Shell (Blue), recorded in 0.5 mol L^{-1} KOH solution. Scan rate of 50 mV s^{-1} at room temperature.

XAS measurements were performed for all electrocatalysts as a function of applied potential in alkaline solutions (Figure 5). First, Figure 5A displays a representative set of spectra obtained at 0.45 V for all synthesized NP structures and the commercially available Pt/C with similar size (~2 nm). The inset plot shows the intensity of the white line corresponding to the Pt d-orbital vacancy. At this potential, it can be observed that the alloy shows a higher white line intensity relative to Pt, while the ordered intermetallic has a lower value. This could be related to a donation of electron density from Ni to Pt. We recorded similar spectra for several electrode potentials within the range of interest for the electrooxidation of the target fuels (Figure S2). We also plotted the measured white

line intensities for each material as a function of electrode potential; Figure 5B presents the corresponding curves. Based on these results, we inferred that the variation in the Pt-Ni atomic arrangements modified the electronic density of Pt, which was clearer at potentials corresponding to surface oxidation. To better relate the results, we will provide a more detailed analysis of the XAS data in light of the fuel electrooxidation experiments.

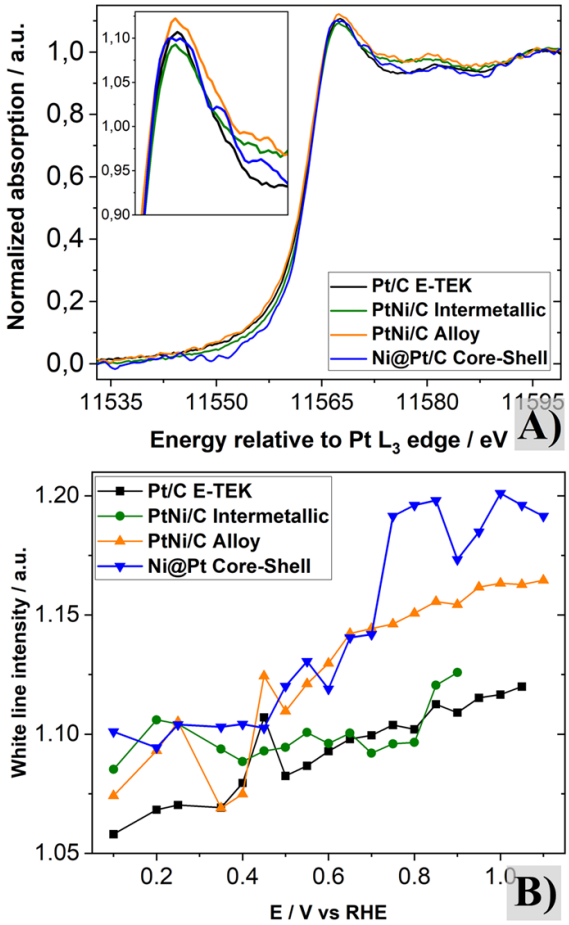

Figure 5 A) XAS Pt L3 near edge spectra recorded for PtNi/C Ordered Intermetallic (Green), PtNi/C Alloy (Orange) and Ni@Pt/C Core-Shell (Blue) and Pt E-TEK (Black) in 0.5 mol L^{-1} KOH solution at room temperature A) at fixed potential of 0.45 V, with the inserted graph zooming into the white line region; and B) Intensities of the white line determined as a function of the potential applied to the electrode.

3.3 Fuels Electrooxidation Evaluation

Here, we detail the performance of the synthesized materials and commercial Pt toward the electrooxidation of hydrogen, methanol, ethanol, ethylene glycol, and glycerol. Figure 6 shows the RDE polarization curves for the hydrogen oxidation reaction (HOR) at the examined surfaces from which we obtained the corresponding Koutecky-Levich plots, presented as insets. Table 1 summarizes the results obtained with the same properties. Considering our hypothesis, we expected the materials to exhibit distinct performances toward the HOR, which was confirmed. The Pt-Ni alloy and ordered intermetallic provided the highest and the lowest kinetic current, respectively. At this point, we did not have enough experimental/theoretical support to explain the

results comprehensively. Nevertheless, it is essential to emphasize that the materials differed only in their structures.

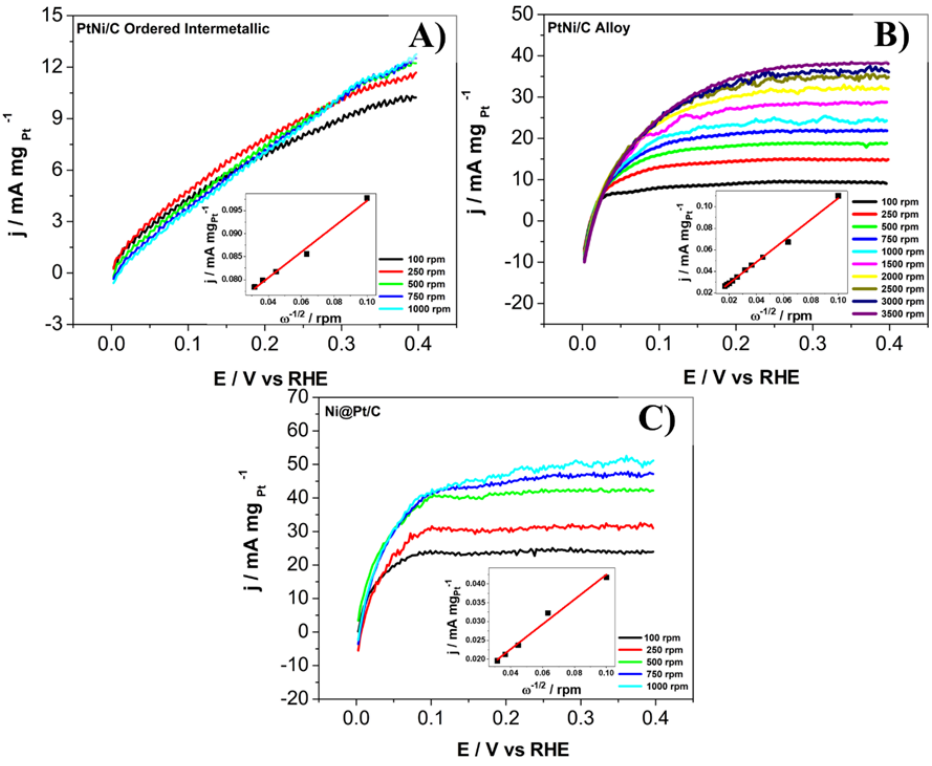

Figure 6 RDE curves for the hydrogen oxidation reaction in 0.5 mol L^{-1} KOH saturated H_2 solution at room temperature for A) PtNi/C Ordered Intermetallic, B) PtNi/C Alloy and C) Ni@Pt/C Core-Shell, as a function of the electrode rotation speed. Inserts show the Koutecky-Levich plots built with the data obtained from the curves.

Table 1 Electrochemical parameters obtained from the hydrogen oxidation reaction (HOR) at distinct surfaces of PtNi systems with distinct configurations in 0.5 mol L^{-1} KOH saturated with H_2 at room temperature.

Fuel	**Pt-Ni Structure**	**RDE**	
		j_k *(mA* mg_{Pt}^{-1}*)*	$C_0.B$ *(mA* mg_{Pt}^{-1} $rpm^{-1/2)}$
Hydrogen	Intermetallic	14.4	3.59
	Alloy	109.1	1.01
	Core-Shell	42.2	3.03

Figure 7 shows representative whole experimental curves obtained for stabilized cycling potential in 0.5 mol L^{-1} + 0.5 mol L^{-1} methanol solution at room temperature. The performance of the nanostructures toward the electrooxidation of organic fuels was also evaluated using a stationary (chronoamperometry - CA) and a potentiodynamic (cyclic voltammetry - CV) technique. We used the cycling potential forward scan and the steady-state current for each applied potential to construct the plots for methanol in Figure 8 for analysis and comparison purposes. The CA and CV curves obtained for all other liquid fuels are presented as Supporting Information (Figures S3-S5). These results reveal the similarity between the curve profiles for the stationary and the

potentiodynamic measurements for each material/fuel set. However, for some nanostructure/fuel sets, we noticed some displacements related to the electrode's potential for each pair of curves. Because such comparison is not usual in the literature, we can infer that the phenomenon could originate from the differences between the processes of adsorption of products/intermediates on the nanostructure's surface taking place along the electrochemical reaction. These adsorption differences could undoubtedly become more evident depending on the time scale of the employed technique. This behavior reinforced the distinct adsorptive characteristic of the surface site, which turned on the electronic condition of the Pt site in each nanostructure.

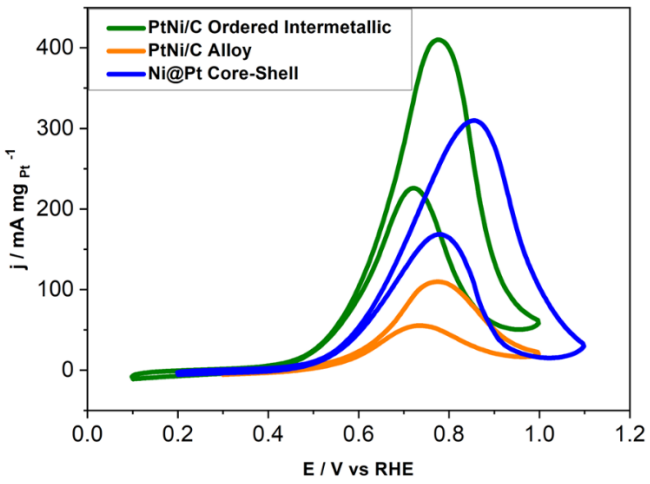

Figure 7 Cyclic voltammograms for PtNi/C Ordered Intermetallic (Green), PtNi/C Alloy (Orange) and Ni@Pt/C Core-Shell (Blue), recorded in 0.5 mol L^{-1} KOH + 0.5 mol L^{-1} methanol solution. Scan rate of 20 mV s^{-1} at room temperature.

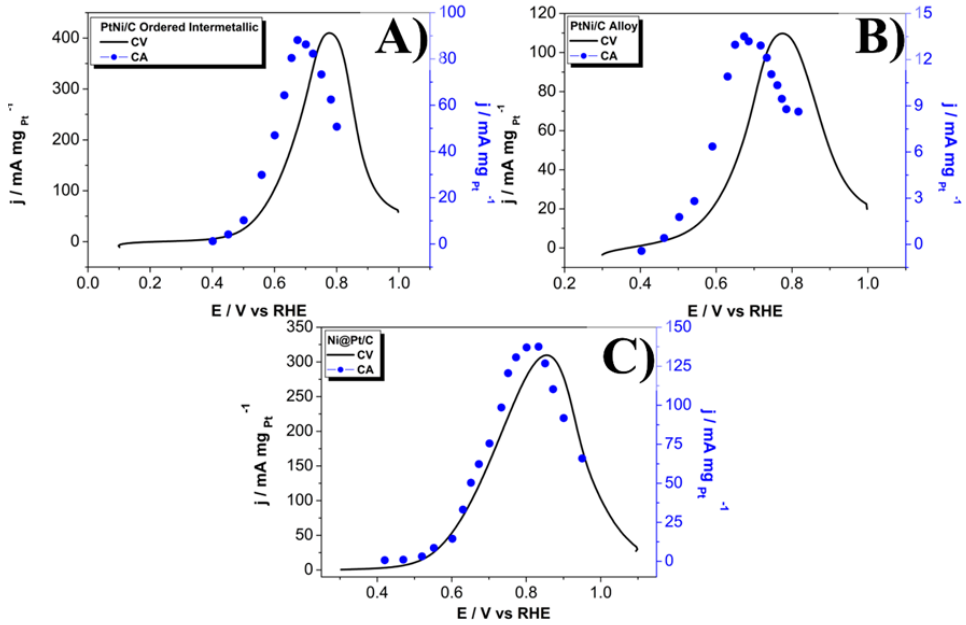

Figure 8 Representative potentiodynamic (lines) and steady-state (blue dots) data registered for electrooxidation in 0.5 mol L^{-1} KOH + 0.5 mol L^{-1} methanol solution at room temperature for A) PtNi/C Ordered Intermetallic, B) PtNi/C Alloy and C) Ni@Pt/C Core-Shell.

Table 2 summarizes the electrochemical parameters collected for all alcohol's electrochemical oxidation on each investigated nanostructure obtained by both electrochemical techniques. A general qualitative coincidence existed between the maximum current reached for each reaction from potentiodynamic and steady-state regimes.

Table 2 Electrochemical parameters obtained from the electrooxidation of different fuels at distinct surfaces of PtNi systems with distinct configurations in 0.5 mol L^{-1} KOH + 0.5 mol L^{-1} fuel at room temperature.

Fuel	Pt-Ni Structure	CV			CA	
		j_p (mA mg_{Pt}^{-1})	Ep (V)	OP (V)	j_p (mA mg_{Pt}^{-1})	Ep (V)
Methanol	Intermetallic	410	0.77	0.56	88	0.67
	Alloy	109	0.77	0.59	13	0.67
	Core-Shell	310	0.85	0.56	138	0.83
Ethanol	Intermetallic	240	0.77	0.48	13	0.82
	Alloy	75	0.64	0.38	5	0.68
	Core-Shell	131	0.72	0.48	11	0.86
Ethylene glycol	Intermetallic	2048	0.99	0.53	410	0.73
	Alloy	1395	0.95	0.57	217	0.71
	Core-Shell	2135	1.00	0.60	295	0.75
Glycerol	Intermetallic	449	0.80	0.44	70	0.74
	Alloy	392	0.77	0.45	50	0.70
	Core-Shell	882	0.91	0.54	106	0.82

4. Discussion

The electrocatalysts were well synthesized and characterized by several techniques in this work. Besides the small particle size, HR-TEM showed well-dispersed NPs at the carbon black support. In addition, the patterns of the diffractograms matched the literature and could be assigned to the designed materials. However, we want to propose a different hypothesis for the core shell here than the ones found in the references. While the displacements in the alloy XRD (Figure 2A) are due to the entry of the smaller Ni atom (1.25 Å) into the Pt (atomic radii of 1.39 Å) lattice interstices, the explanations for the core-shell structure are still unclear in the literature. Chen *et al.* [25] obtained the same Ni@Pt/C material with a similar size but described the shifted peaks at the XRD pattern by slightly increasing the Ni lattice with the deposition of Pt layers at the shell. Testimony of a Pt layer is unlikely to provoke any cell expansion on the previously crystallized Ni lattice. We believe Pt atoms should be deposited on the Ni surface, and the Ni lattice should act as a template. Since α_{FCC} is smaller for Ni (3.52 Å) than for Pt (3.92 Å) [26], the first Pt layers should have decreased α_{FCC}. This cell parameter should approach the usual Pt α_{FCC} the further the coating is from the Ni core. This should also be a reasonable explanation for the mass effect proposed as the reason for peak displacement in the XRD profiles of core-shell NPs. Figure 9 illustrates the phenomenon of Pt lattice contraction and evanescence as a function of the distance to the Ni core.

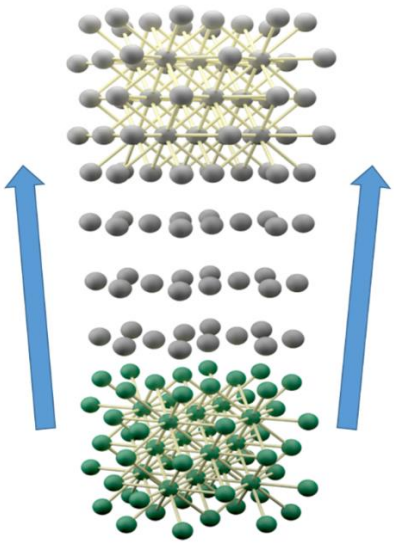

Figure 9 Schematic representation of the mass effect observed during Pt deposition (grey spheres) on the Ni core (green spheres). Arrows indicate the direction of the growing Pt layers. Size and bond proportions correspond to the actual structures of the pure metals.

One of the most essential steps in the electrochemical process is the initial adsorption of the reactant molecules. This step determines the method: the way and the strength through which the reactant molecules adsorb on the electrode will drive the cleavage of the chemical bonds and the formation/desorption of the intermediates and products. In turn, the electronic condition of the adsorption site (Pt atoms) will guide the adsorption step. Our hypothesis previously stated by Equations (1) and (2) established that the structural arrangement of the Pt and Ni atoms, which defines the strength of the interaction between them and consequently the electronic condition of the Pt sites, should strongly influence the adsorption step at first, thereby affecting the whole electrochemical process despite the identical composition of the materials. This is why we have made in-situ measurements using XAS and electrochemical techniques as a basis for contribution to our discussion.

Analysis in the XANES region for the Pt L3 edge depicts the dependence of the intensity of the white line (corresponding to the Pt d-orbital emptying phenomenon) and was also analyzed by varying the electrode potential. Between 0.1 and 0.4 V in Figure 5B, the intensity of the white line varied randomly with the applied potential. This intensity gradually increased to potentials more positive than 0.4 V for all materials due to the interaction between the Pt adsorption site and the species in the electrolyte solution (mainly HO^- ions) and further surface oxidation. The curve of the Ni@Pt/C nanostructure increased markedly at potentials related to the oxide formation on the surface, which suggests that the electronic density tends toward a probable bond with the oxygen atom. Disregarding the random dependence of the white line intensity on the potential in the hydrogen region (0.1-0.4 V), three different behaviors of this intensity related to the possibility of the electrode were evident and could be summarized: a) the ordered intermetallic presented similar values compared to pure Pt NPs; b) the ordinary alloy showed higher intensity compared to pure Pt NPs; and c) the core-shell showed higher values than pure Pt, including a very noticeable increase of the white line intensity at >0.7 V. These behaviors allowed us to interpret how the nanostructure

of the materials impacted the electrooxidation of fuels from the perspective of the electronic condition of the adsorption site on the Pt surface. The electronic condition of the Pt atoms was notably influenced by how the Pt atoms bind to the Ni atoms in each nanostructure. The main effect of the adsorption site on the Pt surface concerned the adsorption characteristics of the species participating in the surface processes. In the initial step of the surface process, the adsorption energy of the reactant molecule at the surface could weaken bonds that would later breakthrough electron transfer. This step strongly depended on the electronic condition of the surface site because this interaction energy should drive the progress of the reaction. Remembering the Volcano plots initially proposed for the HER [29], this energy reaches an optimum value necessary for the weakening step and consequent desorption of the intermediates/products. After the initial electron transfer at the surface, the intermediates and products must be desorbed from the surface to free the adsorption site for a new cycle of steps. During the electrooxidation of organic fuels, a wide range of intermediates and products usually arise. Some constitute surface-blocking species because of their high energy adsorption with the surface adsorption site [18, 21-23]. This should be the main reason for the differences observed during the electrooxidation of fuels at surfaces with the same adsorption site, composition, and particle size but distinct nanostructures.

Recalling Table 1, the PtNi/C alloy performed better toward the HOR. Unfortunately, in this potential region, we cannot reach any conclusive behavior regarding the intensity of the Pt white line observed for the distinct structures, so we cannot reliably establish any relationship between the electronic condition of Pt and the way this atom is bound in the form. On the other hand, considering the energy that is necessary to oxidize the fuel and the rate of the oxidation reaction (respectively represented by the potential and the current density), we were able to verify that the ordered intermetallic PtNi/C structure performed better toward the electrooxidation of methanol and ethanol. In contrast, the Ni@Pt/C core-shell structure showed better results for glycerol electrooxidation. As for ethylene glycol's electrooxidation, the ordered intermetallic and core-shell structures performed as satisfactory electrode materials. Furthermore, as proposed earlier, all reactions were sensitive to the nanostructure of the materials despite the same particle size, chemical identity, composition, and amount of catalysts (available surface area) in said materials.

Despite the significant number of papers devoted to the electronic condition of surface adsorption sites and the performance of materials during electrooxidation reactions, only a few indirect evidences of the relationship between the electronic state of the adsorption site and the structure are available. For example, Gao and co-workers [30] synthesized PtAg pompon-like nanocrystals and evaluated them for the oxidation of ethylene glycol in an alkaline medium. The material presented long-term stability and activity of 5042.9 mA mg^{-1}, 5.4 times greater than commercially available Pt/C. The authors attributed such excellent performance to the bristles at the surface, numerous active surface sites, and synergistic and electronic effects. The authors suggested that the electronic environment around the Pt site changed probably because the charge was transferred between Pt and Ag.

Consequently, this charge transfer inhibited the formation of the intermediate species involving CO at the Pt surface. Kim *et al.* [31] also prepared PtAg nanotubes (PtAgNTs) from the partial galvanic exchange of Pt on Ag in an alkaline medium. They studied the oxidation of glycerol and ethylene glycol on the surface of this material. Their results showed that the PtAgNTs performed better than Pt black, commercial Pt/C, and PtNTs during both reactions. According to the authors, the enhanced performance could result from the structural effects elicited by the Ag incorporated

in Pt. Judging from the XPS measurements, the binding energy of Pt 4f-orbital in the PtAgNTs was lower than the PtNTs, indicating that Pt's electronic structure changed significantly in the presence of the alloy phase PtAg. Xu *et al.* [32] synthesized dendritic PtCu nanocrystals and evaluated their activity during ethylene glycol electrooxidation in an alkaline medium. According to the cyclic voltammetry results obtained by these authors, the material presented excellent performance: the mass activity was 4259.2 mA mg^{-1}, 4.5 times higher than the mass activity of commercial Pt. The XPS spectra of 4f Pt in PtCu shifted positively compared to pure Pt, suggesting that the electronic structure was altered due to slight charge transfer from Cu to Pt during the alloying of dendritic PtCu. The papers above and similar publications have pointed to the electronic condition of the surface adsorption site (usually Pt) as the leading property driving the electrode reaction. However, the conjuncture of the material that succeeded in such an electronic condition has always been laconic. In this context, the present study contributes to this issue by proposing a different approach that could elucidate the surface site's electronic condition based on the area's structural and chemical environment. More than discovering new electrocatalysts, we believe such an approach will significantly improve our understanding of the electrocatalytic process.

To the best of our knowledge, there is not enough data to establish a reliable relationship between the adsorption of reactants, intermediates, and products on Pt sites in different nanostructures, except for the studies cited earlier in this paper. However, this study has shown that the identity of the atoms present in an electrode material and the way they are bonded to each other in the structural arrangement strongly influence the material's performance during electrochemical reactions of interest in fuel cells. Further studies on the same approach could undoubtedly offer a guideline and provide a deeper understanding of the role played by the properties of electrocatalysts in electrochemical processes.

5. Conclusions

We have investigated how the geometric structure of Pt-Ni NPs influences the electrochemical oxidation of hydrogen, methanol, ethanol, ethylene glycol, and glycerol in an alkaline medium. We have evaluated different arrangements of Pt-Ni NPs with the same composition and similar size, namely the ordered intermetallic, ordinary alloy, and core-shell configurations. Our extensive characterization of the synthesized materials has shown that the different structures provide Pt adsorption surface sites with distinct electronic conditions. As a consequence, the NPs perform differently when they are employed as anode material in electrooxidation reactions. We have attributed the particular performances to the different adsorption of the reactants, intermediates, and products on the surface of the tested materials. We believe the methodological approach presented herein contributes to a better understanding of electrocatalysis.

Acknowledgments

In honor to Professor Ernesto R. González.

Author Contributions

Nicolas Ishiki: synthesis and characterization of nanoparticles. Maria Della-Costa: studied of the nanomaterials activities towards the methanol, ethanol and ethylene glycol electrooxidation

reaction. Beatriz Keller: studied the hydrogen oxidation reaction on the nanomaterials surfaces. Kleper Rocha: helped XANES data interpretation. Francielle Bortoloti: studied of the nanomaterials activities towards the glycerol electrooxidation reaction. Antonio Ângelo: adviser, planned and supervised the whole work.

Funding

This work was funded via São Paulo Research Foundation (FAPESP) and National Council for Scientific and Technological Development (CNPq).

Competing Interests

The authors have declared that no competing interests exist

Additional Materials

1. Figure S1: EDX data obtained for A) Ordered Intermetallic, B) Alloy and C) Core-shell nanoparticles at five different points at the particle surfaces. All results in weight %.
2. Table S1: Atomic proportions of the metals in the synthesized materials obtained by conducting EDX analysis at five different points on each sample.
3. Figure S2: XAS Pt L_3 near edge spectra recorded for Pt-Ni nanoparticles materials in the A) Ordered Intermetallic, B) Alloy, and C) Core-Shell configurations as a function of the potential applied to the electrode in 0.5 mol L^{-1} KOH solution at room temperature.
4. Figure S3: Representative potentiodynamic (lines) and steady-state (blue dots) data registered for electrooxidation in 0.5 mol L^{-1} KOH + 0.5 mol L^{-1} glycerol solution at room temperature for A) PtNi/C Ordered Intermetallic, B) PtNi/C Alloy and C) Ni@Pt/C Core-Shell.
5. Figure S4: Representative potentiodynamic (lines) and steady-state (blue dots) data registered for electrooxidation in 0.5 mol L^{-1} KOH + 0.5 mol L^{-1} ethanol solution at room temperature for A) PtNi/C Ordered Intermetallic, B) PtNi/C Alloy and C) Ni@Pt/C Core-Shell.
6. Figure S5: Representative potentiodynamic (lines) and steady-state (blue dots) data registered for electrooxidation in 0.5 mol L^{-1} KOH + 0.5 mol L^{-1} ethylene glycol solution at room temperature for A) PtNi/C Ordered Intermetallic, B) PtNi/C Alloy and C) Ni@Pt/C Core-Shell.

References

1. Alayoglu S, Nilekar AU, Mavrikakis M, Eichhorn B. Ru-Pt core-shell nanoparticles for preferential oxidation of carbon monoxide in hydrogen. Nat Mater. 2008; 7: 333-338. doi: 10.1038/nmat2156.
2. Alayoglu S, Eichhorn B. Rh-Pt bimetallic catalysts: Synthesis, characterization, and catalysis of core-shell, alloy, and monometallic nanoparticles. J Am Chem Soc. 2008; 130: 17479-17486. doi: 10.1021/ja8061425.
3. Liu Z, Jackson GS, Eichhorn BW. PtSn intermetallic, core-shell, and alloy nanoparticles as CO-tolerant electrocatalysts for H_2 oxidation. Angew Chem. 2010; 122: 3241-3244. doi: 10.1002/ange.200907019.

4. Greeley J, Stephens IE, Bondarenko AS, Johansson TP, Hansen HA, Jaramillo TF, et al. Alloys of platinum and early transition metals as oxygen reduction electrocatalysts. Nat Chem. 2009; 1: 552-556. doi: 10.1038/nchem.367.
5. Bao H, Li J, Jiang L, Shang M, Zhang S, Jiang Z, et al. Structure of Pt_nNi nanoparticles electrocatalysts investigated by X-ray absorption spectroscopy. J Phys Chem C. 2013; 117: 20584-20591. doi: 10.1021/jp404799d.
6. Mu R, Fu Q, Xu H, Zhang H, Huang Y, Jiang Z, et al. Synergetic effect of surface and subsurface Ni species at Pt-Ni bimetallic catalysts for CO oxidation. J Am Chem Soc. 2011; 133: 1978-1986. doi: 10.1021/ja109483a.
7. Campos Roldán CA, Calvillo L, Granozzi G, Alonso Vante N. Alkaline hydrogen electrode and oxygen reduction reaction on Pt_XNi nanoalloys. J Electroanal Chem. 2020; 857: 113449. doi: 10.1016/j.jelechem.2019.113449.
8. Xia T, Zhao K, Zhu Y, Bai X, Gao H, Wang Z, et al. Mixed-dimensional Pt-Ni alloy polyhedral nanochains as bifunctional electrocatalysts for direct methanol fuel cells. Adv Mater. 2023; 35: 2206508. doi: 10.1002/adma.202206508.
9. Leonard BM, Zhou Q, Wu D, DiSalvo FJ. Facile synthesis of PtNi intermetallic nanoparticles: Influence of reducing agent and precursors on electrocatalytic activity. Chem Mater. 2011; 23: 1136-1146. doi: 10.1021/cm1024876.
10. Zou L, Fan J, Zhou Y, Wang C, Li J, Zou Z, et al. Conversion of PtNi alloy from disordered to ordered for enhanced activity and durability in methanol-tolerant oxygen reduction reactions. Nano Res. 2015; 8: 2777-2788. doi: 10.1007/s12274-015-0784-0.
11. Bortoloti F, Ishiki NA, Della Costa ML, Rocha KO, Angelo AC. Influence of Pt-Sn system nanostructure on the electronic conditions at a Pt adsorption surface site. J Phys Chem C. 2018; 122: 11371-11317. doi: 10.1021/acs.jpcc.8b01662.
12. Herrero E, Chrzanowski W, Wieckowski A. Dual path mechanism in methanol electrooxidation on a platinum electrode. J Phys Chem. 1995; 99: 10423-10424. doi: 10.1021/j100025a054.
13. Marković NM, Gasteiger HA, Ross Jr PN, Jiang X, Villegas I, Weaver MJ. Electro-oxidation mechanisms of methanol and formic acid on Pt-Ru alloy surfaces. Electrochim Acta. 1995; 40: 91-98. doi: 10.1016/0013-4686(94)00241-R.
14. Sriramulu S, Jarvi TD, Stuve EM. Reaction mechanism and dynamics of methanol electrooxidation on platinum (111). J Electroanal Chem. 1999; 467: 132-142. doi: 10.1016/S0022-0728(99)00036-4.
15. Wilhelm S, Iwasita T, Vielstich W. COH and CO as adsorbed intermediates during methanol oxidation on platinum. J Electroanal Chem Interfacial Electrochem. 1987; 238: 383-391. doi: 10.1016/0022-0728(87)85187-2.
16. Baranova EA, Padilla MA, Halevi B, Amir T, Artyushkova K, Atanassov P. Electrooxidation of ethanol on PtSn nanoparticles in alkaline solution: Correlation between structure and catalytic properties. Electrochim Acta. 2012; 80: 377-382. doi: 10.1016/j.electacta.2012.07.030.
17. Falase A, Main M, Garcia K, Serov A, Lau C, Atanassov P. Electrooxidation of ethylene glycol and glycerol by platinum-based binary and ternary nano-structured catalysts. Electrochim Acta. 2012; 66: 295-301. doi: 10.1016/j.electacta.2012.01.096.
18. Kwon Y, Schouten KJ, Koper MT. Mechanism of the catalytic oxidation of glycerol on polycrystalline gold and platinum electrodes. ChemCatChem. 2011; 3: 1176-1185. doi: 10.1002/cctc.201100023.

19. Lee S, Kim HJ, Choi SM, Seo MH, Kim WB. The promotional effect of Ni on bimetallic PtNi/C catalysts for glycerol electrooxidation. Appl Catal A Gen. 2012; 429: 39-47. doi: 10.1016/j.apcata.2012.04.002.
20. Miecznikowski K. WO_3 decorated carbon nanotube supported PtSn nanoparticles with enhanced activity towards electrochemical oxidation of ethylene glycol in direct alcohol fuel cells. Arab J Chem. 2020; 13: 1020-1031. doi: 10.1016/j.arabjc.2017.09.005.
21. Serov A, Kwak C. Recent achievements in direct ethylene glycol fuel cells (DEGFC). Appl Catal B Environ. 2010; 97: 1-12. doi: 10.1016/j.apcatb.2010.04.011.
22. Sieben JM, Duarte MM. Nanostructured Pt and Pt-Sn catalysts supported on oxidized carbon nanotubes for ethanol and ethylene glycol electro-oxidation. Int J Hydrog Energy. 2011; 36: 3313-3321. doi: 10.1016/j.ijhydene.2010.12.020.
23. Vigier FA, Coutanceau CH, Hahn FR, Belgsir E, Lamy CL. On the mechanism of ethanol electro-oxidation on Pt and PtSn catalysts: Electrochemical and in situ IR reflectance spectroscopy studies. J Electroanal Chem. 2004; 563: 81-89. doi: 10.1016/j.jelechem.2003.08.019.
24. Cable RE, Schaak RE. Low-temperature solution synthesis of nanocrystalline binary intermetallic compounds using the polyol process. Chem Mater. 2005; 17: 6835-6841. doi: 10.1021/cm0520113.
25. Chen Y, Yang F, Dai Y, Wang W, Chen S. Ni@Pt core-shell nanoparticles: Synthesis, structural and electrochemical properties. J Phys Chem C. 2008; 112: 1645-1649. doi: 10.1021/jp709886y.
26. White PS, Rodgers JR, Le Page Y. Crystmet: A database of the structures and powder patterns of metals and intermetallics. Acta Crystallogr Sec B Struct Sci. 2002; 58: 343-348. doi: 10.1107/S0108768102002902.
27. Do CL, San Pham T, Nguyen NP, Tran VQ, Pham HH. Synthesis and characterization of alloy catalyst nanoparticles PtNi/C for oxygen reduction reaction in proton exchange membrane fuel cell. Adv Nat Sci Nanosci Nanotechnol. 2015; 6: 025009. doi: 10.1088/2043-6262/6/2/025009.
28. Callister WD, Rethwisch DG. Materials Science and Engineering: An Introduction, 9th edition. Hoboken, NJ, US: John Wiley & Sons; 2013.
29. Trasatti S. Work function, electronegativity, and electrochemical behaviour of metals: III. Electrolytic hydrogen evolution in acid solutions. J Electroanal Chem Interfacial Electrochem. 1972; 39: 163-184. doi: 10.1016/S0022-0728(72)80485-6.
30. Gao F, Xu H, Zhang Y, Wang J, Wang C, Du Y. Facile construction of pompon-like PtAg alloy catalysts for enhanced ethylene glycol electrooxidation. Int J Hydrogen Energy. 2018; 43: 9644-9651. doi: 10.1016/j.ijhydene.2018.04.005.
31. Kim Y, Kim H, Kim WB. PtAg nanotubes for electrooxidation of ethylene glycol and glycerol in alkaline media. Electrochem Commun. 2014; 46: 36-39. doi: 10.1016/j.elecom.2014.06.007.
32. Xu H, Yan B, Yang J, Li S, Wang J, Du Y, et al. Exceptional ethylene glycol electrooxidation activity enabled by sub-16 nm dendritic Pt-Cu nanocrystals catalysts. Int J Hydrog Energy. 2018; 43: 1489-1496. doi: 10.1016/j.ijhydene.2017.12.016.